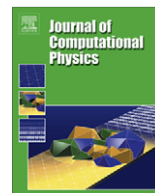




Contents lists available at ScienceDirect

## Journal of Computational Physics

journal homepage: [www.elsevier.com/locate/jcp](http://www.elsevier.com/locate/jcp)

## Simulating the dynamics of flexible bodies and vortex sheets

Silas Alben

School of Mathematics, Georgia Institute of Technology, 686 Cherry Street, Atlanta, GA 30332-0160, United States

## ARTICLE INFO

## Article history:

Received 24 February 2008

Received in revised form 2 December 2008

Accepted 15 December 2008

Available online xxxx

## PACS:

47.11.-j

47.11.Kb

47.32.C-

47.15.ki

46.40.jj

## Keywords:

Implicit

Coupled

Flow-body

Flexible

Vortex sheet

## ABSTRACT

We present a numerical method for the dynamics of a flexible body in an inviscid flow with a free vortex sheet. The formulation is implicit with respect to body variables and explicit with respect to the free vortex sheet. We apply the method to a flexible foil driven periodically in a steady stream. We give numerical evidence that the method is stable and accurate for a relatively small computational cost. A continuous form of the vortex sheet regularization permits continuity of the flow across the body's trailing edge. Nonlinear behavior arises gradually with respect to driving amplitude, and is attributed to the rolling-up of the vortex sheet. Flow quantities move across the body in traveling waves, and show large gradients at the body edges. We find that in the small-amplitude regime, the phase difference between heaving and pitching which maximizes trailing edge deflection also maximizes power output; the phase difference which minimizes trailing edge deflection maximizes efficiency.

© 2008 Elsevier Inc. All rights reserved.

## 1. Introduction

Computing the large-amplitude motions of flexible bodies in fluids is challenging when the Reynolds number (or inverse viscosity) is large. Resolving the flow accurately requires solving for the position and motion of thin layers of vorticity, which can display highly complex dynamics in even the simplest situations. A fundamental source of complexity is the Kelvin–Helmholtz instability, which leads initially flat layers of vorticity to roll up into spirals [1]. The instability growth rate is maximal at large wave numbers, leading to fast growth in the spatial complexity of thin vortex layers [2].

When the motion of the solid boundary is coupled to the fluid dynamics, an additional challenge arises. The boundary conditions for the fluid solver are now to be imposed on a boundary with location unknown *a priori*. The motion of the body and the flow can only be determined together as a coupled system.

The immersed boundary method has been applied to a wide range of problems in this class [3]. The method's generality makes it suitable for a number of problems. The method uses an Eulerian grid in the fluid, a Lagrangian grid on the body, and an interpolation scheme to communicate forces between the two. At large Reynolds numbers, very fine grids are required to resolve vorticity. Furthermore, in standard formulations convergence is formally second-order in space, though practically first-order convergence often occurs [4,5].

E-mail address: [alben@math.gatech.edu](mailto:alben@math.gatech.edu)

A different fluid model considers the infinite Reynolds number limit, in which case the flow is inviscid and irrotational, apart from the vortex layers, which tend to sheets of infinitesimal thickness. Computing the dynamics of isolated vortex sheets in free space began in the 1930s [6], but some of the most fundamental issues in such calculations have been resolved only in the last twenty years [2,7]. These calculations and earlier efforts [8,9] showed that the Birkhoff–Rott equation for the dynamics of a vortex sheet is ill-posed, giving rise to a singularity in the sheet curvature at finite time. Consequently many workers have studied regularized versions of the Birkhoff–Rott equation to obtain smooth problems [10]. Such regularizations have also been used to suppress numerical instabilities [2].

Despite the challenges inherent in the computation of vortex sheets, they are efficient representations of thin shear layers in high Reynolds number flows. They are surfaces in the flow, and hence reduce the dimensionality of the problem by one relative to bulk fluid solvers, which must distribute many grid points across the shear layer.

How vortex sheets are produced at solid surfaces is another challenge which has been addressed recently [11,12], by reformulating the Kutta condition, well-known in classical airfoil theory [13]. These models apply to flows past sharp-edged bodies, which fixes the edge as the location at which the vortex sheet separates from the body. The rate of vorticity flux from the body edge into the sheet is set to make finite the flow velocity at the body edge. Mathematically, this condition removes the singularity which arises generically in potential flow past a sharp-edged body.

Very recently, workers have begun to apply such models to the motions of deforming bodies with prescribed motions [14]. When the body is a flat plate, many of the equations can be formulated analytically. For deforming bodies in prescribed motion, a more general formulation of the equations coupling the body to the flow is required. An additional level of complexity arises when the motion of the deformable body is not prescribed in advance, but is instead coupled to the flow. This is the topic we address here. Because the motion of the body and the strength of vorticity it sheds into the flow are coupled, each can reinforce the other to create a numerical instability unless a special stabilizing approach is found. Here we describe a stable method for such problems, which was recently used to study the large-amplitude dynamics of the flapping-flag instability [15]. The present work examines the numerical method, which was not described in [15]. The present work also gives results in the context of a different problem of scientific interest – the production of vorticity by a passive flexible fin, immersed in an oncoming flow, and driven at the leading edge by a pitching and heaving motion. The linearized version of this problem was studied theoretically in [16], which described some of the basic physics of the generation of thrust forces. Principal among the results was the appearance of an optimal flexibility for thrust, which occurs at the first of a series of resonant-like peaks, each corresponding to an additional half-wavelength of deformation on the fin. In the linearized model, the vortex sheet is a semi-infinite line extending downstream of the fin, and the strength of vorticity on the sheet is simply a travelling wave.

In the general (large-amplitude) version of the problem considered here, the dynamics of the vortex sheet show instead the rolling-up behavior due to the Kelvin–Helmholtz instability. As in the flapping-flag case, the computation is made somewhat easier by the presence of a background flow. The background flow is by no means necessary, but allows for less expensive long-time simulations by moving the vortex sheet steadily away from the body, where the sheet can be approximated by point vortices.

The goal of this work is to describe and present results for a stable and efficient method for coupled vortex sheet-flexible body dynamics, in a fundamental biolocomotion problem. The paper is organized as follows. In Section 2, we present the complete equations for the coupled initial-boundary-value problem consisting of a 2D inviscid flow past a 1D elastic body with a vortex sheet produced at the body’s trailing edge. In Section 3 we present the numerical method for this problem, which combines an implicit formulation on the body with an explicit formulation on the free sheet. We also present results on the behavior of the scheme with respect to numerical parameters. In Section 4, we present results with respect to physical parameters. Section 5 summarizes the main results.

## 2. Flexible body vortex sheet model

We model the tail fin of a swimming fish as a slender elastic filament in a two-dimensional inviscid flow (see Fig. 1). The model fin is an inextensible elastic sheet of length  $2L$ , mass per unit length  $\rho_s$ , and uniform rigidity  $B$ , moving under the pressure forces of a surrounding inviscid and incompressible fluid of density (mass per unit area)  $\rho_f$ . The fin position is  $\zeta(s, t)$ , where  $s$  is arclength;  $-L \leq s \leq L$ . The fin position evolves according to Newton’s 2nd law as a geometrically-nonlinear elastica with inertia [17]:

$$\rho_s \partial_{tt} \zeta(s, t) = \partial_s (T(s, t) \hat{s}) - B \partial_s (\partial_s \kappa(s, t) \hat{n}) - [p](s, t) \hat{n}. \quad (1)$$

Here  $T(s, t)$  is a tension force which maintains inextensibility,  $\kappa(s, t)$  is the fin curvature, and  $[p](s, t)$  is the pressure jump across the fin. We have assumed for simplicity that the rigidity  $B$  is uniform, and defer a consideration of the spatial distribution of  $B$  to future work.

For simplicity we shall represent 2D quantities as complex numbers, so that  $\zeta(s, t) = x(s, t) + iy(s, t)$  is the fin position. Here  $\hat{s}$  and  $\hat{n}$  are complex numbers representing the unit tangent and normal vectors to the fin, respectively. Therefore we have  $\hat{s} = \partial_s \zeta = e^{i\theta(s, t)}$ , where  $\theta(s, t)$  is the local tangent angle, and  $\hat{n} = ie^{i\theta(s, t)}$ . We shall make extensive use of the following identity between the scalar product of two real vectors  $(a, b)$  and  $(c, d)$  and the product of the complex numbers  $w_1 = a + ib$  and  $w_2 = c + id$ :  $(a, b) \cdot (c, d) = \text{Re}(w_1 \bar{w}_2)$ , where the bar denotes the complex conjugate.

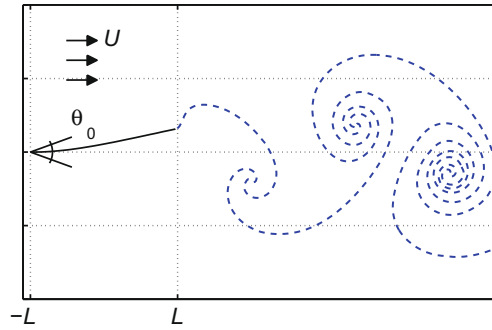


**Fig. 1.** A schematic of a flexible fin of length  $2L$  pitching at the leading edge with amplitude  $\theta_0$  in a steady background flow of speed  $U$ . A vortex sheet (dashed line) emanates from the trailing edge.

We assume that the fin is immersed in a background flow with uniform velocity  $U$  in the far field. The leading edge boundary condition for Eq. (1) is a sinusoidal pitching motion (as if driven by muscles in a fictitious body upstream) with angular frequency  $\omega$ :

$$\zeta(s = -L, t) = -L; \quad \theta(s = -L, t) = \theta_0 \cos(\omega t). \quad (2)$$

The kinematics of a tail fin or bird wing are more accurately modelled by including heaving as well as pitching [18]. Our main interest here is on the thrust as a function of flexibility. We find the optimal rigidity for pitching to be similar to that for pitching plus heaving, because in both cases the bending rigidity is the key parameter which governs how the leading edge motion is transmitted to subsequent sections of the body against fluid resistance. However, in Section 4.1 we shall consider combined heaving and pitching.

Free-end boundary conditions,  $T = \kappa = \partial_s \kappa = 0$ , are assumed at the trailing edge ( $s = L$ ). Scaling lengths on  $L$ , time on  $2\pi/\omega$ , and mass on  $\rho_f L^2$ , the dimensionless fin equation becomes:

$$R_1 \partial_{tt} \zeta = \partial_s (T \hat{s}) - R_2 \partial_s (\partial_s \kappa \hat{n}) - [p] \hat{n} \quad (3)$$

with dimensionless boundary conditions

$$\zeta(-1, t) = -1; \quad \theta(-1, t) = \theta_0 \cos(2\pi t), \quad (4)$$

$$T(1, t) = \kappa(1, t) = \partial_s \kappa(1, t) = 0. \quad (5)$$

The dimensionless parameters are:

- (1)  $R_1 = \rho_s / \rho_f L$ , the dimensionless fin mass.
- (2)  $R_2 = \frac{B}{\rho_f L^2} \left(\frac{2\pi}{\omega}\right)^2$ , the dimensionless fin rigidity.
- (3)  $\theta_0$  = the dimensionless pitching amplitude.
- (4)  $\Omega = \omega L / U$ , the reduced pitching frequency.

The tension is eliminated from Eq. (3) by integration of the  $\hat{s}$ -component from  $s = 1$ , using the boundary condition  $T(1, t) = 0$ :

$$T(s, t) = \int_1^s (R_1 \text{Re}(\partial_{tt} \zeta \bar{\hat{s}}) - R_2 \kappa \partial_s \kappa) ds'. \quad (6)$$

The tail fin is coupled to the flow through the pressure jump in Eq. (3). The flow is modelled as a 2D inviscid flow, with vorticity in the form of a jump in tangential velocity  $\gamma$  along a continuous curvilinear arc. The arc consists of a “bound” vortex sheet on the fin, which separates from the trailing edge into a “free” vortex sheet in the flow (see Fig. 1). This flow model dates to the early days of airfoil theory [13], agrees well with experiments [19,20], and has been used more recently by [21,12,22]. The bound vortex sheet is a model for the two boundary layers on either side of the slender body. In the limit of infinite Reynolds number, the two boundary layers are vortex sheets. In the limit of zero body thickness, the two vortex sheets merge into a single bound vortex sheet.

The complex conjugate of the flow velocity  $(u_x, u_y)$  at any point  $z$  in the flow can be calculated in terms of the vortex sheet strength  $\gamma$  by integrating the vorticity in the bound and free sheets against the Biot–Savart kernel [10]:

$$u_x(z) - i u_y(z) = \frac{2\pi}{\Omega} + \frac{1}{2\pi i} \int_{C_b + C_f} \frac{\gamma(s', t)}{z - \zeta(s', t)} ds'. \quad (7)$$

The first term on the right,  $2\pi/\Omega$ , is the dimensionless flow velocity at infinity, according the nondimensionalization used in Eq. (3). Here  $C_b$  is the contour representing the fin ( $-1 \leq s' \leq 1$ ) and  $C_f$  is the contour representing the free sheet

( $1 \leq s' \leq s_{\max}$ ). We can express the average  $w$  of the flow velocities on the two sides of any point  $\zeta(s, t)$  on  $C_b$  or  $C_f$  by taking the average of the limits of Eq. (7) as  $z$  approaches  $\zeta(s, t)$  from above and below the contours:

$$\bar{w}(s, t) = \frac{2\pi}{\Omega} + \frac{1}{2\pi i} \mathcal{P} \int_{-1}^1 \frac{\gamma(s', t)}{\zeta(s, t) - \zeta(s', t)} ds' + b(s, t), \quad (8)$$

$$b(s, t) = \frac{1}{2\pi i} \mathcal{P} \int_1^{s_{\max}} \frac{\gamma(s', t)}{\zeta(s, t) - \zeta(s', t)} ds'. \quad (9)$$

In Eq. (8),  $\bar{w}$  is the complex conjugate of  $w$ , and the integral is of principal-value type. We can rewrite  $b(s, t)$  in a more convenient Lagrangian form. The free vortex sheet consists of a line of fluid particles which are continually advected away from the trailing end of the fin, for  $t \geq 0$ . Following [12], we define the circulation as the integral of  $\gamma$  over the body and free sheet:

$$\Gamma(s, t) = \int_{s_{\max}}^s \gamma(s', t) ds', \quad -1 < s < s_{\max}. \quad (10)$$

We denote the total circulation in the free sheet by  $\Gamma_+(t) = \int_{s_{\max}}^1 \gamma ds'$ . According to the Helmholtz laws for vorticity conservation in two-dimensional flows, specialized to a vortex sheet,  $\Gamma(s, t)$  is conserved on fluid particles ([10], p. 30):

$$\frac{d}{dt} \Gamma(s, t) = 0, \quad s \in C_f. \quad (11)$$

Here the time derivative is a material derivative, the rate of change following a fluid particle, which moves according to Eq. (13). Thus each fluid particle in  $C_f$  carries the value of circulation  $\Gamma(s, t) = \Gamma(1, t^*)$  it has at the time  $t^*$  when it is “born” at the trailing edge of the fin. We can label material points by  $\Gamma$ , and reparametrize  $b(s, t)$  in Eq. (9) by circulation  $\Gamma$  using  $\gamma ds = d\Gamma$ :

$$b(s, t) = -\frac{1}{2\pi i} \mathcal{P} \int_0^{\Gamma_+(t)} \frac{d\Gamma'}{\zeta(s, t) - \zeta(\Gamma', t)}. \quad (12)$$

On the free vortex sheet  $C_f$ , it can be shown that material points  $\zeta(\Gamma, t)$  move with velocity  $w$  ([10], p.31). This gives the Birkhoff–Rott equation for the evolution of the free vortex sheet:

$$\frac{\partial \bar{\zeta}}{\partial t}(\Gamma, t) = \frac{2\pi}{\Omega} + \frac{1}{2\pi i} \mathcal{P} \int_{C_b} \frac{\gamma(s', t)}{\zeta(s, t) - \zeta(s', t)} ds' + \frac{1}{2\pi i} \mathcal{P} \int_{C_f} \frac{d\Gamma'}{\zeta(\Gamma, t) - \zeta(\Gamma', t)}, \quad \zeta(\Gamma, t) \in C_f. \quad (13)$$

Using  $\Gamma$  to label points on the free sheet eliminates the need for a separate evolution equation for  $\gamma(s, t)$  on the free sheet in Eq. (9). This is the main purpose of using the Lagrangian description of the free sheet here.

We apply Eq. (8) also to  $\zeta(s, t)$  on the fin, to express the kinematic condition that fluid does not penetrate the fin on either side. In other words, the component of the fin velocity normal to the fin equals the same component of  $w$ :

$$\text{Re}(\hat{n} \partial_t \bar{\zeta}(s, t)) = \text{Re}(\hat{n} \bar{w}(s, t)), \quad \zeta(s, t) \in C_b. \quad (14)$$

$$\text{Re}(\hat{n} \partial_t \bar{\zeta}(s, t)) = \text{Re} \left( \hat{n} \left( \frac{2\pi}{\Omega} + \frac{1}{2\pi i} \mathcal{P} \int_{-1}^1 \frac{\gamma(s', t) ds'}{\zeta(s, t) - \zeta(s', t)} + b(s, t) \right) \right), \quad \zeta(s, t) \in C_b. \quad (15)$$

When the left hand side of Eq. (15) and  $b(s, t)$  are known, the general solution  $\gamma(s, t)$  has inverse-square-root singularities at  $s = \pm 1$  [23]. If we define  $v(s, t)$ , the bounded part of  $\gamma(s, t)$ , by

$$\gamma(s, t) = \frac{v(s, t)}{\sqrt{1 - s^2}}, \quad (16)$$

the kinematic condition becomes:

$$\text{Re}(\hat{n} \partial_t \bar{\zeta}(s, t)) = \text{Re} \left( \hat{n} \left( \frac{2\pi}{\Omega} + \frac{1}{2\pi i} \mathcal{P} \int_{-1}^1 \frac{v(s', t) ds'}{\sqrt{1 - s'^2} (\zeta(s, t) - \zeta(s', t))} \right) + b(s, t) \right), \quad \zeta(s, t) \in C_b. \quad (17)$$

A complication arises in using Eq. (13) to solve for the dynamics of a free vortex sheet numerically. The equation is ill-posed, which causes numerical errors to increase rapidly in simulations [7]. Krasny and others showed that the ill-posedness can be removed by modifying the singular kernel in Eq. (13) using a smoothing parameter  $\delta$  [2]. The  $\delta$ -smoothed versions of Eqs. (13) and (17) are:

$$\partial_t \bar{\zeta}(s, t) = \frac{2\pi}{\Omega} + \frac{1}{2\pi i} \mathcal{P} \int_{-1}^1 \frac{\gamma(s', t) ds'}{\zeta(s, t) - \zeta(s', t)} + b_\delta(s, t), \quad \zeta(s, t) \in C_f, \quad (18)$$

$$\text{Re}(\hat{n} \partial_t \bar{\zeta}(s, t)) = \text{Re} \left( \hat{n} \left( \frac{2\pi}{\Omega} + \frac{1}{2\pi i} \mathcal{P} \int_{-1}^1 \frac{v(s', t) ds'}{\sqrt{1 - s'^2} (\zeta(s, t) - \zeta(s', t))} \right) + b_\delta(s, t) \right), \quad \zeta(s, t) \in C_b. \quad (19)$$

respectively, where

$$b_s(s, t) = -\frac{1}{2\pi i} \int_0^{\Gamma_+(t)} d\Lambda' \frac{\overline{\zeta(s, t) - \zeta(\Lambda', t)}}{|\zeta(s, t) - \zeta(\Lambda', t)|^2 + \delta^2}. \quad (20)$$

The instantaneous total circulation in the free sheet,  $\Gamma_+(t)$ , is determined by the Kutta condition, which states that at each time  $t$  the fluid velocity at the trailing edge  $s = 1$  is finite. In particular,  $\gamma$ , which is also the tangential component of the jump in fluid velocity across the fin, must be finite at the trailing edge. Using Eq. (16), the Kutta condition becomes:

$$v(1, t) = 0. \quad (21)$$

At each time  $t$ , Eq. (21) is a constraint which we use to determine  $\Gamma_+(t)$ , as described below in Eq. (38). We also impose the conservation of circulation in the flow (Kelvin's Theorem) as described below in Eq. (37). This condition equates  $\Gamma_+(t)$  to the integral of  $\gamma$  on the body for a flow started from rest, which we shall consider here.

One can relate the pressure jump across the fin  $[p]$  to the vortex sheet strength along the fin by a version of the unsteady Bernoulli equation. One writes the Euler equations for fluid velocities at points above and below the fin, and takes the limit that the points approach each other from opposite sides of the fin (see [10,12]). The difference of these equations is an evolution equation for the difference of the fluid velocities, which is  $\gamma \hat{s}$  (the normal component is zero by the no-penetration condition on either side of the fin). The evolution equation for the vortex sheet strength  $\gamma$  is [12]:

$$\gamma_t + \partial_s((\mu - \tau)\gamma) = \partial_s[p]. \quad (22)$$

where  $\tau(s, t)$  is the tangential component of the fin velocity and  $\mu(s, t)$  is the tangential component of the average fluid velocity:

$$\tau(s, t) = \text{Re}(\partial_t \zeta(s, t) \bar{\hat{s}}); \quad \mu(s, t) = \text{Re}(w(s, t) \bar{\hat{s}}). \quad (23)$$

The pressure jump across the free sheet is zero, which yields the boundary condition for Eq. (22),

$$[p]|_{s=1} = 0. \quad (24)$$

We integrate Eq. (22) along  $C_b$  to determine  $[p](s, t)$  on the fin,  $-1 < s < 1$ .

We present here the full system of unknowns and corresponding equations:

$$\begin{aligned} \zeta(s, t), s \in C_b, -1 \leq s \leq 1 : \text{Eq. (3)}, \\ v(s, t), s \in C_b : \text{Eq. (19)}, \\ [p](s, t), s \in C_b : \text{Eqs. (22) and (16)}, \\ \zeta(s, t), s \in C_f, 1 \leq s \leq s_{\max} : \text{Eq. (18)}, \\ \Gamma(s, t) = \Gamma(1, t^*), s \in C_f : \text{Eq. (21)}. \end{aligned} \quad (25)$$

Because the fin is nearly aligned with the flow, we neglect separation upstream of the trailing edge – in particular, at the leading edge – and allow the flow velocity and pressure to diverge as the inverse square-root of distance from the leading edge. The divergent pressure creates a finite leading-edge suction on the body which is a reasonable model for the force in the actual flow [10], and is a standard component of classical models for flows past slender airfoils [13].

We wish to solve the set of nonlinear singular integrodifferential Eqs. (25) for large-amplitude motions of flexible bodies coupled to vortex sheets. For general boundary conditions, a numerical solution is required. A similar set of equations was solved by Jones and Shelley, numerically, for a rigid flat plate undergoing a prescribed motion [12,24]. In those works it was shown that the Kutta condition could be rewritten in terms of the circulation flux by integrating Eq. (22) over the free sheet. A linearized version of the equations for an infinite body with no free sheet was used by Shelley et al. to compute normal modes of a flapping-flag [25]. The large-amplitude version of that problem was recently treated with the method described here [15].

The main quantities of physical interest to us and previous workers ([26–28]) are the instantaneous input power applied to the fin  $P_{in}$  (the rate of work done per unit time at the leading edge), and the output power  $P_{out}$ . These are:

$$P_{in} = -R_2 \kappa \left. \frac{\partial \theta}{\partial t} \right|_{s=-1} \quad (26)$$

$$P_{out} = \frac{\pi^2}{4\Omega} v^2 \cos \theta \Big|_{s=-1} + \frac{2\pi}{\Omega} \int_{-1}^1 [p] \sin \theta ds \quad (27)$$

The first term on the right hand side of Eq. (27) is a suction force due to the inverse-square-root flow singularity at the leading edge. This is the limit of the suction force on a leading edge of small but finite radius of curvature, in the limit that the radius tends to zero (i.e. the body becomes sharp-edged) [10]. Eq. (26) is the rate of work done to create the pitching motion and is equal to the moment applied at the leading edge  $-R_2 \kappa$  times the angular velocity there. The output power is defined as the rate of work done per unit time by thrust forces on the fin, which is the thrust force times the velocity of the fluid stream  $2\pi/\Omega$ . This form of  $P_{out}$  was used by [26] and many others in the ‘‘Froude efficiency.’’

The main novelty in the model presented in this section is the combination of the elastica Eq. (3) for large-amplitude deformations of a body with previously-studied equations for the dynamics of free vortex sheets. The combination of body bending with vortex sheet dynamics requires a new numerical method which couples the flow and body dynamics.

### 3. Numerical method

Here we give our numerical method for the solution of the system of nonlinear singular integrodifferential Eqs. (25). We solve for the dynamics of the fin at each time step, starting from an initial time  $t_0$  at which the fin is straight, at rest, and the bound vortex sheet has zero strength. The free vortex sheet is initialized as a single point at the trailing edge of the fin, with zero circulation. Each subsequent time step  $t_1, t_2, \dots$ , consists of an *explicit* solution of Eq. (18) followed by an *implicit* solution of the remaining four equations in system (25). An implicit solution of the Birkhoff–Rott equation (18) would be considerably more expensive, because about  $O(10^3)$  variables are needed to represent the free sheet, versus  $O(10^1 - 10^2)$  for the body. The main cost in the implicit portion of the scheme is the matrix-vector multiplications in Broyden's method (explained below), which require  $O(N^2)$  flops where  $N$  is the number of variables. Making the vortex sheet portion of the method implicit would thus increase the flop count per Broyden step by at least  $O(10^2 - 10^4)$ . We would also expect the number of iterations to convergence to increase because the condition number of the Jacobian matrix used in Broyden's method would increase.

Because all variables in the implicit and explicit systems are coupled, we should not expect that making part of the system implicit will necessarily improve the stability of the scheme. Our original intention in solving some of the equations implicitly was to make the formulation simpler. Indeed, it is difficult to formulate a numerical method which is explicit in time, because the highest (second) time derivatives of body position appear not only in the body inertia (left hand side of Eq. (3)), but also in the pressure jump ( $[p]$  in Eq. (3)), through the term  $\partial_t \gamma$  (Eq. (22)), and Eq. (15) which relates  $\gamma$  to body velocity through an integral transform. The implicit treatment we use here uses an iterative method, which requires only matrix-vector multiplications rather than the direct solution of a linear system of equations. However, many possible formulations were found to lead to numerical instability. The coupling between the body and the flow – the fact that larger body motions lead to larger fluid forces and vice versa – seems to underlie many of the instabilities. These are characterized by an exponential growth in variables with respect to time step, and do not seem related to any physical instability. Furthermore, the convergence of the implicit solver for the equations  $\mathbf{F}(\mathbf{x}) = 0$  depends strongly on the conditioning of the Jacobian matrix (the matrix with entry  $(i, j)$  equal to  $\{\partial_{x_j} F_i\}$ ). Some formulations lead to a Jacobian matrix with large condition number. Through a series of educated guesses we have found a partitioning of the equations into explicit and implicit form which is numerically stable and has a well-conditioned Jacobian matrix. This is the scheme we describe now. Future work will consider more systematically why some schemes are stable and some are unstable for this problem.

Numerical method:

- (1) Given at time  $t_0$ : position  $\zeta(s, t_0)$  and velocity  $\partial_t \zeta(s, t_0)$  of body, initial bound vortex sheet strength  $\{\gamma(s, t_0), -1 < s < 1\}$ , and position of free sheet labelled by circulation  $\zeta(\Gamma, t_0)$ .  
(We assume in the examples here flow starting from rest, so that  $\partial_t \zeta(s, t_0)$  and  $\gamma(s, t_0)$  are zero. The free sheet is a point coinciding with the trailing edge (it has zero length and zero circulation).
- (2) For  $k = 1, 2, \dots$ 
  - (a) Explicit method for the free vortex sheet (Section 3.1 below).  
Given at time  $t_{k-1}$ : position  $\zeta(s, t_{k-1})$  and velocity  $\partial_t \zeta(s, t_{k-1})$  of body, bound vortex sheet strength  $\{\gamma(s, t_{k-1}), -1 < s < 1\}$ , and positions of free sheet points labelled by circulation  $\zeta(\Gamma, t_{k-1})$ .  
Output: New positions of free sheet points labelled by circulation  $\zeta(\Gamma, t_k)$ .
  - (b) Implicit method for the body variables (Section 3.2 below).  
Given body variables at time  $t_{k-1}$ :  $\zeta(s, t_{k-1}), \partial_t \zeta(s, t_{k-1}), \{\gamma(s, t_{k-1}), -1 < s < 1\}$ , and position of free sheet labelled by circulation at time  $t_k$ , from step 2a:  $\zeta(\Gamma, t_k)$ . Also given: “clamp” boundary conditions for body leading edge position at time  $t_k$ :  $\zeta(s = -1, t_k), \theta(s = -1, t_k)$ . Free-end boundary conditions are assumed at the trailing edge:  $\kappa(s = 1, t_k) = \partial_s \kappa(s = 1, t_k) = 0$ .  
Output: Body variables at time  $t_k$ :  $\zeta(s, t_k), \partial_t \zeta(s, t_k), \{\gamma(s, t_k), -1 \leq s \leq 1\}$ .

In step 2b, the clamp boundary conditions are prescribed for the body leading edge. We modify Eq. (4) and the background flow to increase the smoothness of the startup. Specifically, we multiply  $\theta_0 \cos(2\pi t_k)$  and the background flow  $2\pi/\Omega$  by a factor  $(1 - e^{-(t_k/0.1)^2})$ , which ensures that the body is initially at rest, with vortex sheet strength zero on the body and in the flow. The exponential factor ensures that the acceleration and its first time derivative are finite. The body reaches a quasi-periodic state rapidly (variables are periodic to within 1% by  $t = 5$  pitching periods). We now describe the explicit and implicit methods of step 2 in detail.

#### 3.1. Explicit method for the free vortex sheet

We first describe the explicit solution of Eq. (18). At time step  $t_{k+1}$  the free sheet consists of  $k + 1$  points, one of which – the newly-created point  $\zeta_k^f(t_{k+1})$  – coincides with the body trailing edge  $\zeta(1, t_{k+1})$ . Here the superscript  $f$  is for “free” vortex sheet. The remaining  $k$  points  $(\zeta_j^f(t_{k+1}), j = 0, \dots, k - 1)$ , created on the previous  $k$  time steps, extend into the flow. The newly-created point is moved to its new position using the local velocity at time  $t_k$ , by the Forward Euler method, and the remaining  $k$  points are moved to their new positions using the local velocities at times  $t_k$  and  $t_{k-1}$  using a second-order explicit Adams–Bashforth method:

$$\begin{aligned}\zeta_k^f(t_{k+1}) &= \zeta_k^f(t_k) + (t_{k+1} - t_k) \partial_t \zeta(s, t)|_{\zeta=\zeta_k^f, t=t_k} \\ \zeta_j^f(t_{k+1}) &= \zeta_j^f(t_k) + (t_{k+1} - t_k) \times (C_1 \partial_t \zeta(s, t)|_{\zeta=\zeta_j^f, t=t_k} + (1 - C_1) \partial_t \zeta(s, t)|_{\zeta=\zeta_j^f, t=t_{k-1}}), \quad j = 0, \dots, k-1 \\ C_1 &= ((t_k + t_{k+1})/2 - t_{k-1}) / (t_k - t_{k-1}).\end{aligned}\tag{28}$$

The constant  $C_1$  makes the second equation accurate to second-order in time. Because the newly-created point at  $s_k$  does not exist at prior times, we do not have velocity or position information at prior times. Hence we use the simplest one-step method, the first-order Euler method. Empirically we find that relative errors are  $O(10^{-2})$  for time steps of  $O(10^{-2})$  (in units of pitching periods) – see Table 2. Because each point is evolved for one time step with the Forward Euler method and for the remaining time steps with the second-order method, the global temporal accuracy is significantly better than if a first-order scheme were used exclusively. A higher-order scheme is possible using higher-order Runge–Kutta methods, but we do not pursue this here.

### 3.2. Implicit method for the body variables

Having updated the free sheet to its position at time  $t_{k+1}$ , we update the body position and bound vortex sheet strength to their values at time  $t_{k+1}$  using an implicit scheme. We use the familiar quasi-Newton method for solving a nonlinear system of equations known as Broyden’s method [29]. We write our system of equations for the implicit solver only – (3), (19), (21), and (22) – in the form

$$\mathbf{F}(\mathbf{x}) = 0.\tag{29}$$

The unknowns  $\mathbf{x}$  for this system are values of  $v$  (defined in Eq. (16)) and  $\kappa$  on  $m + 1$  Chebyshev–Lobatto nodes in  $-1 < s < 1$ , and the total circulation  $\Gamma_+$ :

$$\begin{aligned}x_j &= v(s_j, t_{k+1}), \quad j = 1, \dots, m+1 \\ x_{j+m+1} &= \kappa(s_j, t_{k+1}), \quad j = 1, \dots, m+1 \\ x_{2m+3} &= \Gamma_+(t_{k+1}). \\ s_j &= -\cos(j-1)\pi/m, \quad j = 1, \dots, m+1.\end{aligned}\tag{30}$$

The values  $\mathbf{F}$  in the corresponding  $2m + 3$  nonlinear equations are computed as follows. We start by integrating the curvature  $\kappa(s_j, t_{k+1})$  twice to obtain the body position  $\zeta(s_j, t_{k+1})$ , using the “clamp” boundary conditions (4). We then obtain  $\hat{s}$ , and  $\hat{n}$  using the discrete differentiation matrix of first-order on Chebyshev–Lobatto nodes,  $D_s^1$  (see [30]). The matrix is dense, but because the number of nodes  $m + 1$  is typically small ( $\approx O(10^2)$ ), multiplication by this matrix is computationally inexpensive. A uniform discretization would allow sparse differentiation matrices, but then we would need to interpolate from data on a uniform mesh to data on a Chebyshev mesh, which increases the condition number of the Jacobian matrix  $\partial F_j / \partial x_i$ , slowing convergence.

Using  $\zeta$  (the body position) at previous time steps we compute  $\text{Re}(\hat{n} \partial_t \bar{\zeta}(s_j, t_{k+1}))$  to second-order temporal accuracy. We obtain  $b_\delta(s_j, t_{k+1})$  by performing the integral over the free sheet in Eq. (20) by trapezoidal quadrature. We are now in a position to compute  $v$  as the solution to the integral equation (19). This solution is accomplished in a few stages.

We first split the kernel multiplying  $v$  in Eq. (19) into a singular Cauchy kernel plus a smooth part  $K$ , using the relation:

$$\frac{1}{\zeta(s, t) - \zeta(s', t)} = \frac{1}{\partial_s \zeta(s, t)} \frac{1}{s - s'} + \frac{1}{\partial_s \zeta(s, t)} K(s, s', t), \quad s \neq s'\tag{31}$$

By expanding  $\zeta(s', t)$  in a Taylor series about  $s' = s$ , we can evaluate  $K$  exactly at the singularity:

$$K(s, s', t) = i \frac{\kappa(s, t)}{2}, \quad s = s'\tag{32}$$

so Eq. (19) becomes:

$$\text{Re}(\hat{n} \partial_t \bar{\zeta}(s, t)) = \text{Re} \left( \hat{n} \left( \frac{2\pi}{\Omega} + \frac{1}{2\pi i} \partial_s \zeta(s, t) \int_{-1}^1 \frac{v(s', t) ds'}{\sqrt{1-s'^2}(s-s')} + \frac{1}{2\pi i} \int_{-1}^1 K(s, s', t) \frac{v(s', t) ds'}{\sqrt{1-s'^2}} + b_\delta(s, t) \right) \right), \zeta(s, t) \in C_b.\tag{33}$$

Eq. (33) can be solved for  $v$  using a Chebyshev expansion. We define

$$f(s, t) = \text{Re} \left( \hat{n} \left( -b_\delta(s, t) - \frac{2\pi}{\Omega} + \partial_t \bar{\zeta}(s, t) - \frac{1}{2\pi i} \int_{-1}^1 K(s, s', t) \frac{v(s', t) ds'}{\sqrt{1-s'^2}} \right) \right)\tag{34}$$

and approximate  $f$  by a finite Chebyshev series, which converges rapidly for smooth functions [31]:

$$f(s, t) = \sum_{k=0}^n f_k(t) \cos(k\phi), \quad s = \cos(\phi)\tag{35}$$

The solution  $v$  is then [32]:

$$v(s, t) = 2 \sum_{k=1}^n f_k(t) \sin(\phi) \sin(k\phi) - f_1(t) - 2f_0(t)s + C(t). \quad (36)$$

The term  $C(t)$  is determined by the conservation of circulation (Kelvin's Theorem) for a flow started from rest:

$$\int_{-1}^1 \frac{v(s, t)}{\sqrt{1-s^2}} ds + \Gamma_+(t) = 0 \Rightarrow C(t) = \frac{\Gamma_+(t)}{\pi}. \quad (37)$$

Using Eqs. (36) and (37) we can write the Kutta condition (21) as:

$$-f_1 - 2f_0 + \frac{\Gamma_+(t_{k+1})}{\pi} = 0. \quad (38)$$

Having computed each of the quantities in Eq. (33), we now place it in our system of nonlinear equations:

$$F_i(\mathbf{x}) = v(s_i, t_{k+1}) - 2 \sum_{j=1}^n f_j(t_{k+1}) \sin(j\phi_i) + f_1 + 2f_0 s_i - \frac{\Gamma_+(t_{k+1})}{\pi}, \quad i = 1, \dots, m+1 \quad (39)$$

Next, we form the terms in the beam equation (3). We compute  $\mu$  from Eq. (23), using Eq. (33) with  $\hat{s}$  instead of  $\hat{n}$ . We then compute  $[p]$  by integrating Eq. (22) with boundary condition (24). Another term in the beam equation (3) is  $\partial_{tt}\zeta$ , which we compute with second-order accuracy in time using the values of  $\zeta$  at times  $t_{k+1}$ ,  $t_k$ ,  $t_{k-1}$ , and  $t_{k-2}$ . We compute the tension by inserting  $\kappa(s_j, t_{k+1})$  into Eq. (6). Having formulated all the terms in the beam equation, we now consider how to include boundary conditions for the beam in our system of equations.

The inverse-square-root singularity in  $\gamma$  at the leading edge  $s = -1$  appears also in  $[p]$ , and thus in  $\partial_s^4 \zeta$  through Eq. (3). This does not pose a significant problem, since we omit the boundary-value of Eq. (3) at the leading edge in the nonlinear system. We adopt the standard approach of including in our system of equations Eq. (3) evaluated on the interior nodes only. Since Eq. (3) is second-order in  $\kappa$ , we replace the equations on the two boundary nodes  $s_1, s_{m+1}$  with the two free-end boundary conditions  $\kappa(s_{m+1}, t_{k+1}) = \partial_s \kappa(s_{m+1}, t_{k+1}) = 0$ . The equations we add to our system of nonlinear equations corresponding to the beam equation are then

$$\begin{aligned} F_{j+m}(\mathbf{x}) &= R_1 \text{Re}(\partial_{tt}\zeta(s_j, t_{k+1}) \bar{\tilde{n}}) + D_s^2(R_3 \kappa(s_j, t_{k+1})) - T(s_j, t_{k+1}) \kappa(s_j, t_{k+1}) + [p](s_j, t_{k+1}), \quad j = 2, \dots, m \\ F_{2m+1}(\mathbf{x}) &= \kappa(s_{m+1}, t_{k+1}) \\ F_{2m+2}(\mathbf{x}) &= D_s^1 \kappa(s_{m+1}, t_{k+1}) \end{aligned} \quad (40)$$

Here  $D_s^1$  and  $D_s^2$  are the discrete differentiation matrices of first and second-order on Chebyshev–Lobatto nodes [30]. The last equation in our nonlinear system is the Kutta condition (38):

$$F_{2m+3}(\mathbf{x}) = -f_1 - 2f_0 + \frac{\Gamma_+(t_{k+1})}{\pi}. \quad (41)$$

Broyden's method requires an initial guess at each time step  $t_{k+1}$ , which we provide at second-order by extrapolating from the solutions at the two previous time steps  $t_{k-1}, t_k$ . Having the solution  $\mathbf{x}$  at each time step, we can compute the instantaneous input power  $P_{in}$ , and output power  $P_{out}$  produced by the body (Eqs. (26) and (27)). We now assess the dependence of results on the main numerical parameters. This numerical method has also been validated with the corresponding linearized solutions in the appendix of [16], which examines the linearized problem.

### 3.3. Tapered $\delta$ -smoothing

A difficulty in computing vortex sheets shed from sharp edges is how to reconcile the regularization on the free vortex sheet (Eq. (20)) with the absence of regularization on the bound vortex sheet. (Regularizing the bound vortex sheet would make the integral equation (19) ill-posed). If the regularization parameter  $\delta$  is uniform on the free sheet, the  $\delta$ -smoothed integral in Eq. (19) ( $b_\delta$ , Eq. (20)) is bounded as  $s \rightarrow 1$ . However, the non-smoothed integral in Eq. (19) possesses a logarithmic singularity proportional to  $\gamma(s = 1)$ , which must therefore vanish for Eq. (19) to hold as  $s \rightarrow 1$ . Consequently,  $\gamma$  possesses a jump discontinuity at the trailing edge:  $\gamma$  tends to 0 as  $s$  tends to one from below (moving along the body to its trailing edge), and then abruptly jumps to a nonzero value at the beginning of the free sheet. See previous works for further discussion of this phenomenon [11,21,12,24,14].

Because the details of vortex-shedding are essential to this problem, we have employed a gradual  $\delta$ -smoothing on the free vortex sheet to avoid the discontinuity in  $\delta$  and its effect on the vortex shedding process. We make  $\delta$  in Eq. (20) a function of arc length  $s$  along the free sheet, where  $s = 1$  at the body trailing edge:

$$b_\delta(s, t) = -\frac{1}{2\pi i} \oint_0^{\Gamma_+(t)} d\Lambda' \frac{\zeta(s, t) - \zeta(\Lambda', t)}{|\zeta(s, t) - \zeta(\Lambda', t)|^2 + \delta(\Lambda')^2}, \quad (42)$$

$$\delta(\Lambda') = \delta_0(1 - e^{-|s(\Lambda')-1|^2/\epsilon^2}). \quad (43)$$

Here  $\delta$  tends to zero quadratically with distance from the body's trailing edge. The scale over which  $\delta$  tends to zero is given by  $\epsilon$ . In the simulations presented here  $\epsilon$  is set to 0.2. This value is chosen as a balance of two considerations. Larger  $\epsilon$  is advantageous for moving the region of  $\delta$ -smoothing further away from the body's trailing edge. Smaller  $\epsilon$  is advantageous by limiting the growth of numerical errors in the sheet as it moves through the region of size  $\epsilon$  in which  $\delta$  is small (see [2,7]).

In Table 1 we present results for three different  $\delta_0$ , and find that the maximum differences between quantities (the differences between the quantities for  $\delta_0 = 0.2$  and 0.05) are of the order of 1–4%. By contrast, with  $\delta$  uniform and equal to  $\delta_0$ , these differences range from 20% to 50%. Information on the convergence of vortex sheet dynamics with respect to  $\delta_0$  may be found in [7].

### 3.4. Adaptive time-stepping

We employ adaptive time-stepping to enforce small relative changes in the solution between time steps. Second-order backward differentiation formulae are used for all time derivatives in the implicit solver. The second-order Adams–Bashforth method is used to advance the free sheet explicitly in time. At each time step we compute the relative difference between the current solution  $\mathbf{x}_{k+1}$  and the initial guess of the current solution  $2\mathbf{x}_k - \mathbf{x}_{k-1}$ , extrapolated at second order from the two previous time steps. If the relative difference exceeds a tolerance  $\tau$  (0.003 in the results below) we multiply the time step by 0.95, a decrease of 5%. If the relative difference is smaller than  $\tau/3$ , we multiply the time step by 1.05. In Table 2 we give results with respect to  $\tau$ , and find that the relative difference between all quantities is less than 2% moving from average time step 0.0109 to 0.0053.

### 3.5. Point vortex approximation

For computational efficiency, it is advantageous to focus resolution near the body. An approximation method which we use in this work is to approximate the free vortex sheet by point vortices when it has moved sufficiently far from the body. By dropping second and higher-order terms in the multipole expansion of the approximated sheet, this method incurs an error which is  $O(r^{-2})$  in the velocities induced at the body by the approximated sheet, where  $r$  is the distance between the body and the approximated sheet. In practice, we approximate based on the arc length of the free sheet, computed at regular time intervals. We convert the portion of the free sheet with arc length exceeding a constant  $L_s$  into a point vortex located at the center of vorticity of the replaced portion. The strength of the point vortex is equal to the total vorticity in the replaced portion. The number of point vortices grows in time, but much more slowly than the number of mesh points in the free sheet, since many mesh points are absorbed into a single vortex. When there are many point vortices, clusters of point vortices can be replaced by a single point vortex at the center of vorticity of the cluster. Essential to this approximation is a background flow, which ensures that, once created, point vortices are advected away from the body.

The number of mesh points representing the free sheet remains bounded at long times, because as more points are introduced at the trailing edge of the body, points at the downstream end of the sheet are absorbed into a point vortex. This saturation in mesh points is usually reached after 3–5 pitching periods for the computations considered here.

**Table 1**

Maximum trailing edge deflection over periods 10 to 15 ( $|y|_{\max}$ ), maximum shed circulation over periods 10 to 15 ( $|\Gamma|_{\max}$ ), time-averaged input power, output power, and efficiency  $\eta = \langle P_{out} \rangle / \langle P_{in} \rangle$ , versus the vortex sheet smoothing parameter  $\delta_0$ . The other parameters are:  $R_2 = 100$ ,  $\Omega = \pi$ ,  $\theta_0 = 10$  degrees,  $L_s = 12$ ,  $m = 40$ ,  $\tau = 0.003$ .

$\delta_0$	$ y _{\max}$	$ \Gamma _{\max}$	$\langle P_{in} \rangle$	$\langle P_{out} \rangle$	$\eta$
0.2	0.410	4.24	17.84	4.88	0.274
0.1	0.402	4.21	17.67	4.74	0.268
0.05	0.394	4.26	17.50	4.63	0.265

**Table 2**

Maximum trailing edge deflection over periods 10 to 15 ( $|y|_{\max}$ ), maximum shed circulation over periods 10 to 15 ( $|\Gamma|_{\max}$ ), time-averaged input power, output power, and efficiency  $\eta$ , versus the relative error bound  $\tau$ . The other parameters are:  $R_2 = 100$ ,  $\Omega = \pi$ ,  $\theta_0 = 10$  degrees,  $L_s = 10$ ,  $m = 40$ ,  $\delta_0 = 0.2$ .

$\tau$	$\langle \Delta t \rangle$	$ y _{\max}$	$ \Gamma _{\max}$	$\langle P_{in} \rangle$	$\langle P_{out} \rangle$	$\eta$
1	0.124	0.357	4.31	15.73	3.80	0.241
0.2	0.055	0.385	4.09	16.68	4.12	0.247
0.1	0.036	0.387	4.01	16.91	4.17	0.247
0.03	0.0204	0.388	4.13	17.15	4.36	0.253
0.01	0.0109	0.392	4.19	17.40	4.52	0.260
0.005	0.0070	0.394	4.24	17.47	4.59	0.263
0.003	0.0053	0.394	4.24	17.47	4.61	0.264

**Table 3**

Maximum trailing edge deflection over periods 10 to 15 ( $|y|_{\max}$ ), maximum shed circulation over periods 10 to 15  $|\Gamma|_{\max}$ , time-averaged input power, output power, and efficiency  $\eta$ , versus the length of the non-truncated portion of the vortex sheet  $L_s$ . The other parameters are:  $R_2 = 100$ ,  $\Omega = \pi$ ,  $\theta_0 = 10$  degrees,  $m = 40$ ,  $\tau = 0.003$ ,  $\delta_0 = 0.2$ .

$L_s$	8	10	12	15	20	30
$r$	2.13	2.29	2.76	3.22	3.78	4.71
$ y _{\max}$	0.394	0.393	0.394	0.394	0.394	0.394
$ \Gamma _{\max}$	4.28	4.24	4.31	4.24	4.24	4.26
$\langle P_{in} \rangle$	17.47	17.57	17.52	17.47	17.48	17.52
$\langle P_{out} \rangle$	4.60	4.66	4.63	4.61	4.61	4.64
$\eta$	0.264	0.265	0.265	0.264	0.264	0.265

**Table 4**

Maximum trailing edge deflection over periods 10 to 15 ( $|y|_{\max}$ ), maximum shed circulation over periods 10 to 15  $|\Gamma|_{\max}$ , time-averaged input power, output power, and efficiency  $\eta$ , versus the number of Chebyshev modes  $m$ . The other parameters are:  $R_2 = 100$ ,  $\Omega = \pi$ ,  $\theta_0 = 10$  degrees,  $L_s = 10$ ,  $\tau = 0.003$ ,  $\delta_0 = 0.2$ .

$m$	$ y _{\max}$	$ \Gamma _{\max}$	$\langle P_{in} \rangle$	$\langle P_{out} \rangle$	$\eta$
20	0.403	4.24	17.04	4.48	0.263
40	0.394	4.25	17.57	4.66	0.265
60	0.399	4.19	17.74	4.71	0.266
80	0.399	4.14	17.76	4.72	0.266

For larger  $L_s$ , the minimum distance between the body and the truncated sheet,  $r$ , increases. Therefore, we expect the error in this approximation to decrease as  $L_s$  increases. In Table 3, we give results with respect to  $L_s$  and  $r$ , and find little variation even when the point vortices are as little as one body length from the trailing edge. The relative insensitivity of forces with respect to  $L_s$  indicates that the vorticity production is dominated by the flow near the body, particularly at the trailing edge. We find that  $r$  increases slowly with  $L_s$ . The reason is that the vortex sheet continually rolls up in time, so that the marginal increase in  $L_s$  required to resolve the far wake increases moving away from the body.

### 3.6. Convergence with respect to number of Chebyshev modes

Table 4 shows convergence with respect to  $m$ , the number of Chebyshev modes. We find 1–2% differences between quantities at  $m = 40$  and  $m = 80$ . Due to the square-root behavior of  $\gamma(s, t)$  at the fiber's trailing edge (see [12]), the Chebyshev modes decay algebraically, not exponentially, with mode number.

## 4. Results with respect to physical parameters

We begin by considering the effect of all three physical parameters on the overall performance of the flexible foil: bending rigidity ( $R_2$ ), pitching amplitude ( $\theta_0$ ), and pitching frequency ( $\Omega$ ). Period-averaged power-in and power-out are computed by averaging over 10 periods, starting five pitching periods after  $t = 0$ . By that time and subsequently, the flow is very nearly periodic (all quantities in the tables are periodic to less than 0.5% in relative norm).

In Fig. 2, we give results for 3.5 decades in bending rigidity, four values of pitching amplitude, and two values of pitching frequency (panels 'a' and 'b'). First we examine variations in  $R_2$ . We see two peaks in  $\langle P_{out} \rangle$  and  $\langle P_{in} \rangle$  with respect to  $R_2$ , the highest located above 100, and a smaller peak located near 2. For  $R_2$  above the higher peak, power flattens out as the rigid plate limit is approached. In Fig. 3 we show fiber positions and flows corresponding to these peaks. A linearized analysis [16] has shown that these peaks are resonances, and occur at rigidities  $R_2$  which yield an eigensolution to the coupled system of equations. That analysis shows that when  $\Omega$  tends to infinity, there is an infinite series of peaks, one for each eigensolution, which corresponds approximately to a series of sinusoidal solutions at each half-odd-integer wavelength of bending deformation. At finite  $\Omega$ , terms in the system of equations proportional to  $1/\Omega$  (advection forces) yield a damping of the resonant peaks. Meanwhile, the efficiency ( $\eta = \langle P_{out} \rangle / \langle P_{in} \rangle$ ) decreases from about 50% at small  $R_2$  to 20% at larger  $R_2$ .

We now consider the behavior with respect to  $\theta_0$ , the pitching amplitude. The behavior can be summarized as a multiplicative increase in the power curves with each factor of two increase in  $\theta_0$ . At small  $R_2$ , where response is small, power rises by a factor of four, corresponding to the fact that the expressions for power in Eqs. (26) and (27) are proportional to  $\theta_0^2$  for small  $\theta_0$ . Near the maximum-power  $R_2$  (about 200), the input power rises somewhat more quickly with  $\theta_0$ , showing the emergence of nonlinear effects. A main source of nonlinearity is that the geometry of the vortex wake feeds back on the shed vortex sheet strength. The efficiency is nearly constant with  $\theta_0$  for small  $R_2$ , because the solution lies in the linear regime. At larger  $R_2$ , the efficiency decreases with increasing  $\theta_0$ , because in the nonlinear regime, the input power rises more quickly than does the output power. Finally, we consider the effect of  $\Omega$ . The two peaks in power are damped in panel 'b' relative to panel 'a'. Panel 'b' has smaller  $\Omega$ , corresponding to a faster oncoming flow. At larger  $\theta_0$ , the damping results in an increased efficiency by moving closer to the small-amplitude (linear) regime.

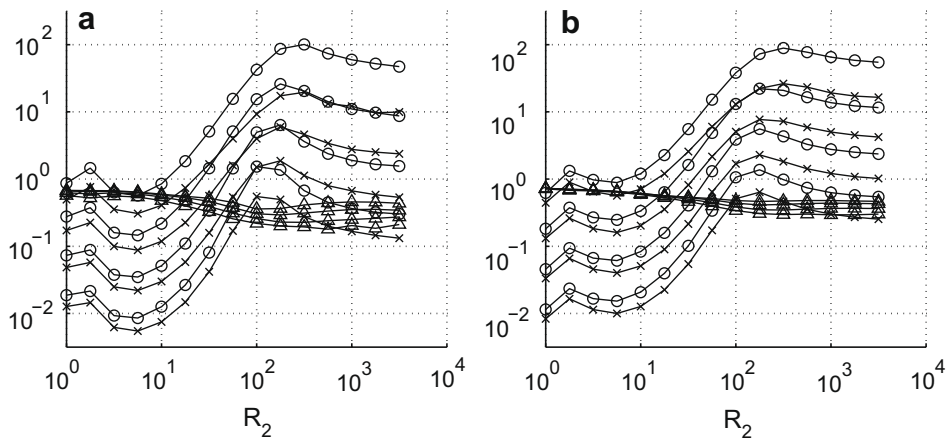


**Fig. 2.** The time-averaged thrust power (crosses), input power (circles), and efficiency (triangles), versus rigidity  $R_2$ , for two pitching frequencies:  $\Omega = 2\pi$  (a) and  $\Omega = 2\pi/3$  (b). Curves are plotted for four pitching amplitudes  $\theta_0 = 2, 4, 8,$  and  $16$  degrees, and increase monotonically with  $\theta_0$ .

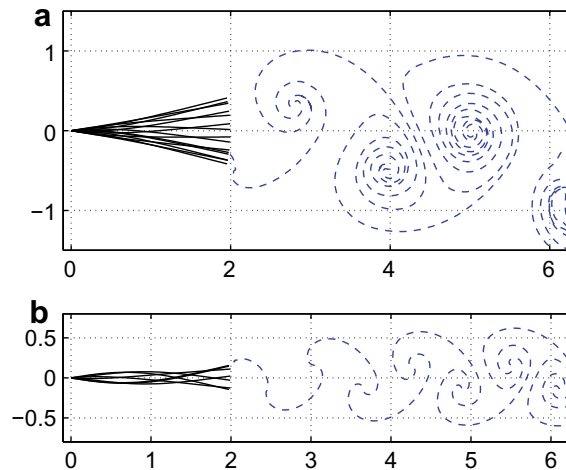


**Fig. 3.** A series of foil snapshots, and instantaneous vortex wakes for frequency  $\Omega = 2\pi$ , and pitching amplitude  $\theta_0 = 10$  degrees, at rigidities corresponding to the first two peaks in thrust in Fig. 2a: (a)  $R_2 = 100$  and (b)  $R_2 = 1.78$ .

In Fig. 3 we show snapshots of foil positions and flows corresponding to the two resonant peaks of Fig. 2(a). In both cases, the vortex sheets roll up into the familiar von Karman vortex street. The higher-thrust case (panel ‘a’) has vortices which are considerably larger and have more spiral turns. This is a result of the larger vorticity they have when leaving the trailing edge. The snapshots indicate that the foil corresponding to the lower-thrust peak is a higher-wavelength mode.

We examine the transition from linear to nonlinear behavior in Fig. 4. We briefly set aside our discussion of flexibility here, and focus on a nearly rigid plate ( $R_2 = 10^4$ ). In the rigid limit we can examine how nonlinearity arises from the evolution of the vortex sheet alone, without the additional effect of body deflection. Shown are the free vortex sheets for eight different pitching amplitudes: ranging from one-half degree, well within the linear regime, to 18 degrees, where fully-separated flow can occur for steady airfoils. In certain cases oscillation can prevent fully-separated flow, and allow for useful lift forces to be obtained beyond the stall angle (i.e. “delayed stall”) [33]. Thus we may expect our assumption that separation is confined to the trailing edge to hold above the classical stall angle  $\approx 15$  degrees for a slender airfoil in *steady* flow [1]. The vortex sheet wake occupies an envelope which grows moving downstream from the body and with  $\theta_0$ . Owing to the inverse-distance dependence of velocity on a vorticity distribution, and the fact that vorticity of alternating sign is produced, the effect of alternating vortex pairs decays like the *square* of inverse-distance from the body. Thus the portion of the vortex sheet nearest the trailing edge is dominant over the remainder of the sheet in affecting the flow on the body. This portion is nearly flat at small  $\theta_0$ , and the rolling-up which occurs downstream is a relatively weak source of nonlinearity. However, at the larger  $\theta_0$  in Fig. 4(g) and (h), the vortex sheet begins to roll up almost immediately upon being shed, and the feedback of this stronger rolling-up on the vorticity being shed is a strengthened nonlinearity.

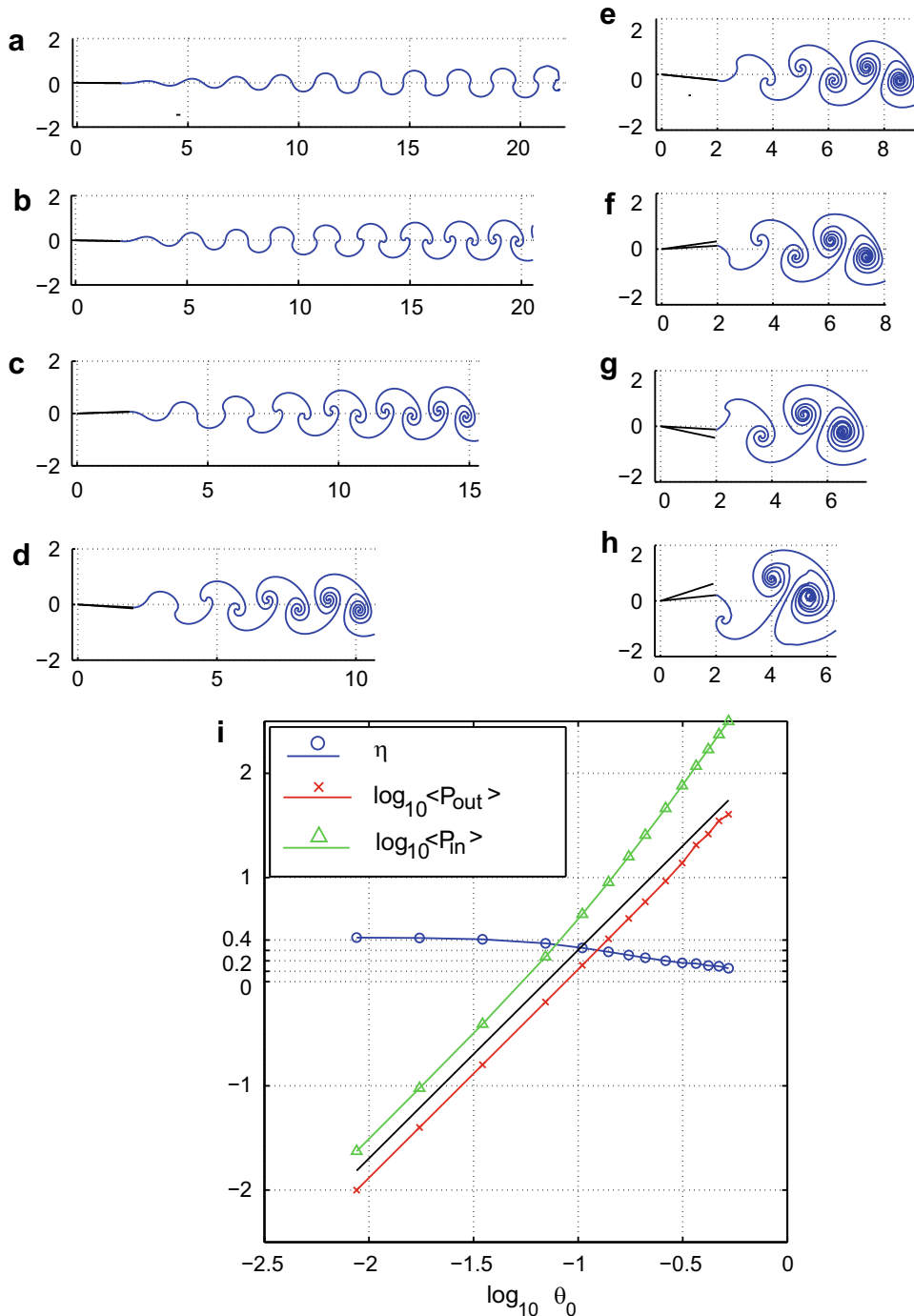


**Fig. 4.** The vortex wakes past a rigid fiber ( $R_2 = 10^4$ ) for increasing values of the pitching amplitude  $\theta_0$ : (a) 0.5 (b) 1 (c) 2 (d) 4 (e) 8 (f) 10 (g) 15 (h) 21 degrees. In each plot, a second black line shows the fiber at maximum amplitude. The time-averaged input and output power and efficiency for various  $\theta_0$  are shown in panel (i). The other parameters are:  $\Omega = \pi$ ,  $\delta_0 = 0.2$ ,  $L_s = 40$ ,  $m = 40$ ,  $\tau = 0.003$ .

In Fig. 4(i) we plot the dependence of time-averaged input power, output power, and their ratio, the “Froude efficiency”  $\eta$ , on  $\theta_0$ . As defined in Eqs. (26) and (27), both input and output power scale as  $\theta_0^2$  for small  $\theta_0$ . This is seen in Fig. 4(i) for  $P_{in}$  up to  $\theta_0 \approx 10$  and for  $P_{out}$  up to  $\theta_0 \approx 20$ . The relatively delayed appearance of nonlinearity in  $P_{out}$  is surprising. We might expect that because the input power is applied at the leading edge, it is therefore somewhat removed from the nonlinear feedback of the shed sheet at the trailing edge. One possible cause of the nonlinearity in input power is the influence of the shed vortex

sheet on the vertical momentum of the fluid upstream, against which the pitching motion works. However, we have no reason to expect that the output power would be less strongly affected by nonlinearities in the flow at the trailing edge.

So far we have focused on the foil and the free vortex sheet. In Fig. 5 we plot the instantaneous streamlines for the flow around a very rigid fiber (a,  $R_2 = 10^4$ ) and a very flexible fiber (b,  $R_2 = 3 \times 10^{-4}$ ), in a reference frame where the fluid is at rest at infinity. For the rigid fiber, we see a ribbon of streamlines which passes between the vortices as an undulating jet. The extent of the influence of the vortex wake is visible in the streamlines outside of the vortex sheet wake. The vertical extent of the eddies is approximately twice the width of the vortex sheet wake itself. For the more flexible fiber (b), the body and wake are nearly indistinguishable in their effect on the streamlines. Both support a series of eddies with diameter approximately one-half fiber length. Here the transition in flow from the trailing edge of the fiber to the wake is very smooth. The effect of leading edge suction on the fiber is noticeable in the presence of an eddy there. In panel 'c' we show a contour plot of flow speed for this case, which reveals a smaller-scale flow structure along the fiber, though not on the free vortex sheet. The reason is that the fiber shape has a small high-wavelength component, due to the smallness of its bending rigidity. Because this component is small, taking the limit that bending rigidity tends to zero yields essentially the same shape. The dominant forces in setting the fiber shape are its inextensibility and the fluid forces. In particular, the fluid advection force appears to damp out high-wavelength fiber shapes. By contrast, if we take the limit that advection speed  $U$  goes to zero (i.e.  $\Omega \rightarrow \infty$ ), the high-wavelength modes of fiber shape instead become dominant [16].

The small high-wavelength component becomes clearer when we examine the fluid pressure difference on the fiber itself. This is shown in Fig. 6(a), together with the fiber shape and the component of fiber velocity normal to itself. We plot six snapshots at equal instants in time over one half cycle. We see that although the fiber shape is relatively smooth, the velocity and pressure show high-frequency oscillations. These oscillations move forward along the fiber as a travelling wave. In the full system of equations, the pressure is dependent on instantaneous fiber position, velocity and acceleration. While the position and acceleration (not shown) are relatively smooth, the velocity has high-frequency components which arise in the pressure. The behavior of flow quantities at the fiber endpoints is also interesting. In Fig. 6(b) we again plot six snapshots over a half cycle, but for rigidity  $R_2 = 100$ , near the maximum thrust value. In place of the normal component of velocity we now plot the (bound) vortex sheet strength on the fiber,  $\gamma$ . At the leading edge, there is an inverse-square-root singularity in the pressure and  $\gamma$ . At the trailing edge, both have a square-root behavior. Unlike in earlier works on vortex-shedding,  $\gamma$  is nonzero at the trailing edge, and continuous with the vortex sheet strength on the free sheet. The pressure distribution falls steeply at the trailing edge, particularly at instants of large trailing edge acceleration. However, the pressure jump changes gradually on the interior of the body, and is nearly spatially uniform at the initial and final times.

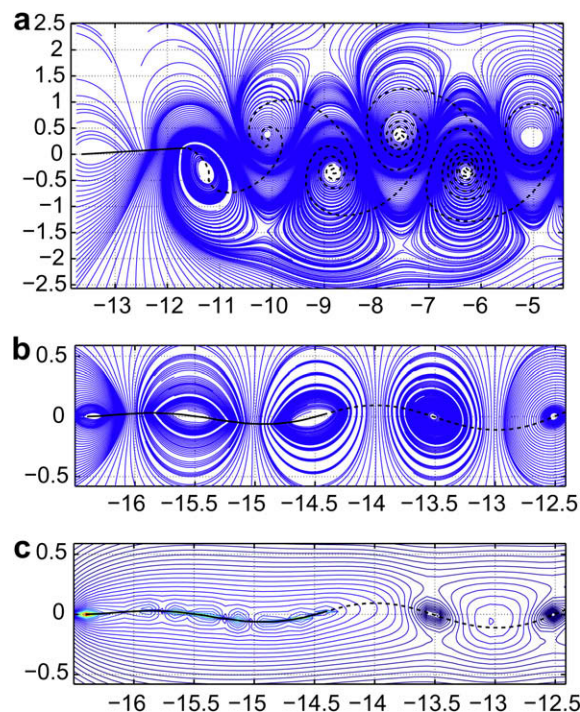


**Fig. 5.** Instantaneous streamlines for the flow speed past (a) a rigid fiber ( $R_2 = 10^4$ ) with  $\theta_0 = 8$  degrees. The streamlines (b) and flow speed contours (c) are plotted for a very flexible fiber ( $R_2 = 0.0003$ ) with  $\theta_0 = 15$  degrees. In both cases  $\Omega = \pi$ .

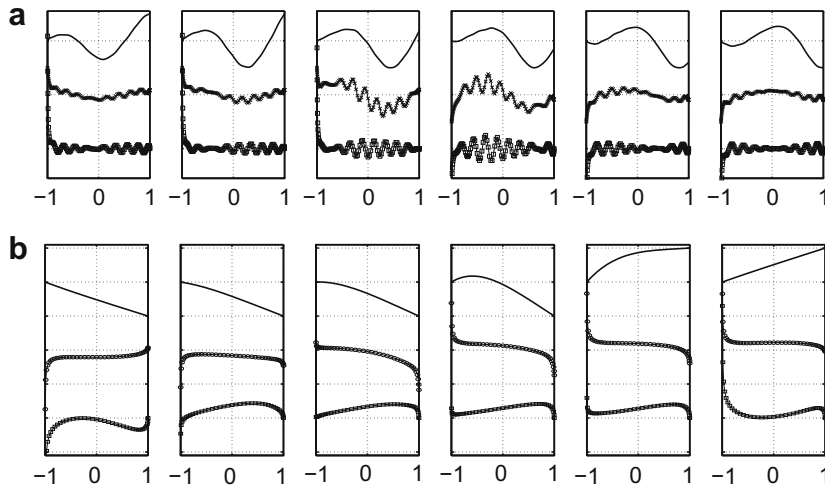


**Fig. 6.** (a) Snapshots of fiber position (solid line), normal velocity (crosses), and fluid pressure (squares) over a half cycle of pitching motion, for a very flexible fiber ( $R_2 = 3 \times 10^{-4}$ ) with  $\theta_0 = 15$  degrees and  $\Omega = \pi$ . (b) Snapshots of fiber position (solid line), vortex sheet strength  $\gamma$  (circles), and fluid pressure (squares) over a half cycle of pitching motion, for a fiber with rigidity near the maximum thrust value ( $R_2 = 100$ ) with  $\theta_0 = 10$  degrees and  $\Omega = \pi$ . In 'b' the vertical amplitude of fiber shape is scaled by its maximum for visibility. In both panels the normal velocity and fluid pressure are divided by four times their mean to make the distribution more visible.

#### 4.1. Combined heaving and pitching

We have so far concentrated on pitching motions alone. A more realistic set of dynamics includes also a periodic transverse motion – “heaving” [18], again considered to be imposed at the leading edge. We assume the heaving has the same frequency as the pitching, and thus change Eq. (4) to

$$\zeta(-1, t) = iy_0 \cos(2\pi t + \phi); \quad \theta(-1, t) = \theta_0 \cos(2\pi t). \quad (44)$$

We have introduced two new parameters: the amplitude of heaving  $y_0$  and the phase shift with respect to pitching  $\phi$ . These are added to the three-parameter space of  $R_2$ ,  $\theta_0$  and  $\Omega$  already studied to yield a five-parameter space. For simplicity we focus on small deflections from alignment with the free stream, so that  $\theta_0 \ll 1, y_0 \ll 1$ . In particular, we choose  $\theta_0$  equal to  $1/4$  degree. The heave-to-pitch ratio  $y_0/\theta_0$  is then varied together with the other three-parameters  $R_2$ ,  $\Omega$ , and  $\phi$ .

We must also update Eq. (26) for the input power to include the work done by heaving, which equals the product of the vertical force applied at the leading edge times the heaving velocity there. The vertical force is the vertical components of the shear force applied to a beam  $R_2 \partial_s \kappa$  [34] and of the suction force from the fluid at the leading edge:

$$P_{in} = -R_2 \kappa \frac{\partial \theta}{\partial t} \Big|_{s=-1} + R_2 \partial_s \kappa \frac{\partial y}{\partial t} \cos \theta \Big|_{s=-1} + \frac{\pi^2}{4\Omega} v^2 \sin \theta \Big|_{s=-1}. \quad (45)$$

Most experimental [35,28] and theoretical studies [36–38] have focused on the case of a rigid plate or foil. Phase angles near  $\phi = 3\pi/2$  (with heaving leading pitching) are commonly observed in carangiform (or tail-dominant) swimming and bird flight [18]. Experiments on rigid foils have found  $\phi = 1.6\pi$  is optimal for thrust within certain parameter regimes [28]. These works are focused on large-amplitude motions and on thrust generation, whereas here we stay within the limit of small deflections from the free stream, and consider efficiency as well as thrust.

In Fig. 7, we fix heaving-to-pitching amplitude ratio at 0.1 and plot contours of the phase  $\phi/\pi$  which maximizes average output power ( $P_{out}$ ), with respect to the two remaining unfixed parameters: reduced frequency  $\Omega$  and rigidity  $R_2$ . Due to the expense of scanning a large portion of parameter space, the contours are based on data with a resolution of four points per decade along each axis. This resolution is sufficient to capture the variation in phase. We find that the classical phase difference of  $1.5\pi$  is favored at small frequencies (or large free stream velocities). At larger rigidities and small frequencies (to the upper left of the dashed line), only drag is possible. As the driving frequency increases, the optimal phase for power output shifts to  $2\pi$ , so that pitching and heaving are in phase. We consider an example in this regime subsequently. First, we note that the optimal phase depends only weakly on bending rigidity, which is somewhat surprising. Also interesting is that these results are nearly identical for heave-to-pitch amplitudes ranging from  $10^{-3}$  to 10, with deviation only between approximately 3 and 10. In the limit of large  $R_2$  (the rigid plate), the trajectory of the entire plate is known given only the phase and the heave and pitch amplitudes. In this case, the phase  $\phi = 2\pi$  has the property of maximizing the maximum trailing edge deflection of the body over a cycle, which determines output power in linearized theories [26,39].

We now focus on a particular, though representative case:  $R_2 = 100$  and  $\Omega = 11.2$ . The rigidity leads to a moderate flexing of the body (Fig. 8(a)) superposed on the rigid plate motion. The reduced pitching frequency is approximately  $4\pi$ , which

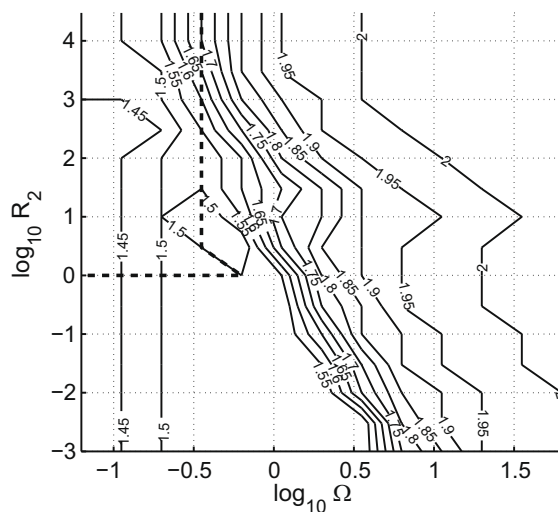


**Fig. 7.** For fixed heave-to-pitch amplitude 0.1, contours of the phase difference  $\phi/\pi$  (Eq. (43)) between heaving and pitching which maximizes output power  $\langle P_{out} \rangle$  (Eq. (27)). In the region to the upper left of the dashed line, the maximum  $\langle P_{out} \rangle$  is negative.

means that the body completes one cycle of flapping in the time for the oncoming fluid to traverse the body streamwise. The heave-to-pitch amplitude ratio is one. In Fig. 8(a) we show snapshots of the body over a cycle in the phase yielding optimal thrust,  $\phi = 0$ . This phase maximizes the displacement at the trailing edge, due to the outward flexing of the body. The resulting trajectory is similar to that of Fig. 3(a). Fig. 8(b) shows the same body at the phase  $\phi = 0.95\pi$  giving maximum Froude efficiency  $\langle P_{out} \rangle / \langle P_{in} \rangle$ . This phase also corresponds to minimum thrust and minimum trailing edge displacement. High efficiency arises for small thrust because relatively little energy is lost to the vortex sheet wake.

We now consider the phase for maximum efficiency over a large portion of parameter space, for the rigid plate only ( $R_2 = 10^4$ ). Having fixed rigidity, in Fig. 9(a), we plot the contours of  $\phi/\pi$  corresponding to maximum Froude efficiency  $\langle P_{out} \rangle / \langle P_{in} \rangle$ , as a function of the two remaining parameters: reduced frequency  $\Omega$  and heave-to-pitch amplitude  $y_0/\theta_0$ . For maximum  $\eta$ , we find that the classical stroke of  $1.5\pi$  is favored only for small pitching frequencies (or large free stream velocity). However, at these parameter values, the thrust force on the body is negative – i.e. drag – for all pitching frequencies.

As  $\Omega$  is increased, there is a smooth transition to phase  $0.8\pi$ , when  $\Omega \approx 2\pi$ ; here the pitching period is of the order of the time for fluid to pass streamwise along the body. When heaving amplitude becomes of the same order as pitching amplitude, the contours change significantly so that phases between  $0.5\pi$  and  $\pi$  – with pitching leading heaving – are favored at all reduced frequencies. The resulting trajectories are similar to those of Fig. 8(b).

In Fig. 9(b), we plot the relative difference between the minimum and maximum efficiencies over all phases. When heaving amplitude is small, the relative phase of heaving is relatively unimportant, so the differences are small. The large change in the contours at smaller  $\Omega$  occurs because positive thrust is no longer possible, so the maximum efficiency tends to zero at the dashed line, and is negative in the region bounded by the dashed line.

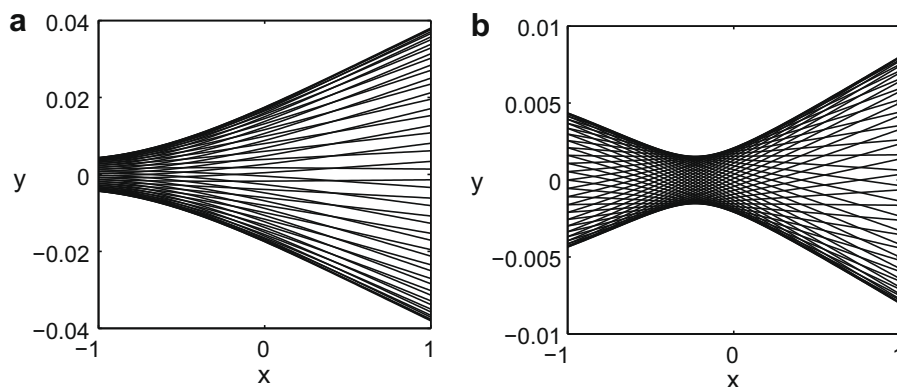


**Fig. 8.** For rigidity  $R_2 = 100$ , heave-to-pitch amplitude ratio 1, and  $\omega = 11.2$ , snapshots of body deflection over a cycle for the phases corresponding to (a) maximum thrust,  $\phi = 0$ , and (b) maximum efficiency (and minimum thrust),  $\phi = 0.95\pi$ .

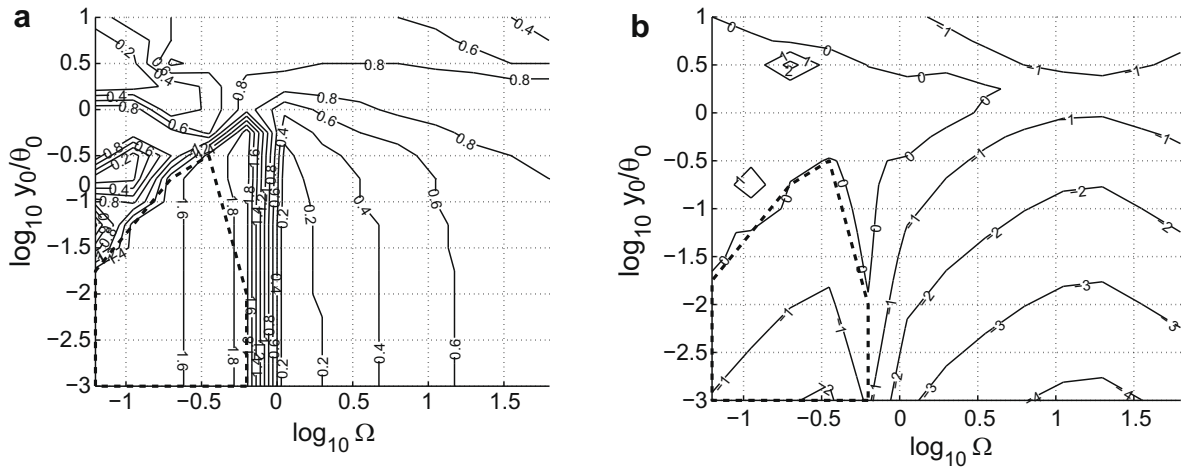


**Fig. 9.** a, Contours of the phase difference  $\phi/\pi$  (Eq. (43)) between heaving and pitching which maximizes Froude efficiency  $\eta = \langle P_{out} \rangle / \langle P_{in} \rangle$  (Eqs. (26) and (27)) for a nearly rigid plate  $R_2 = 10^\circ$ . The horizontal axis is reduced pitching frequency, and the vertical axis is heave-to-pitch amplitude ratio. Pitching amplitude is  $1/4$  degree, giving the small deflection limit. In the region to the lower left of the dashed line,  $\langle P_{out} \rangle$  is negative for all phases. b, Contours of the logarithm (base 10) of the relative difference between maximum and minimum efficiency across all phases. In the region to the lower left of the dashed line,  $\langle P_{out} \rangle$  is negative for all phases.

To summarize the results of this section, we have found that in the limit of small deflection from alignment with the fluid stream, the phases for maximum thrust and maximum efficiency are often opposite or nearly opposite. Maximum thrust is obtained when heaving combines with pitching to generate a larger trailing edge deflection. Maximum efficiency occurs when the two nearly cancel in their effect on the trailing edge displacement.

## 5. Summary and conclusions

We have presented a new numerical method for computing the fully-coupled motions of flexible bodies and vortex sheets. We have computed results for a problem relevant to biolocomotion – a pitching flexible foil in a uniform stream. This problem has been studied previously in the linearized limit [16], which provides a context for some of the results with respect to physical parameters. In addition to the full coupling of flexibility to vortex sheet motion, an important component of this work is the incorporation of gradual increase of vortex sheet smoothing parameter  $\delta$  at the trailing edge. This avoids the large errors at the trailing edge ( $O(1)$  in the limit of small mesh spacing), including jump discontinuities in pressure and vortex sheet strength, which occur otherwise. For parameters corresponding to maximum foil thrust, numerical evidence is presented which indicates accuracy with respect to numerical parameters. Both the mathematical analysis of the well-posedness of the model and the numerical analysis of the stability of possible schemes for coupled flexible body vortex sheet problems are left to future work.

We find that nonlinear behaviors of the input and output power arise gradually with respect to driving amplitude, and may be attributed to the feedback between the rolling-up of the vortex sheet and the flow on the fiber which creates the vortex sheet. Pressure and vortex sheet strength vary rapidly at the trailing edge of the body, which emphasizes the benefit of a gradual onset of vortex sheet smoothing near the trailing edge. We have studied heaving combined with pitching in the small-amplitude regime, with a focus on the phase differences which maximize power output and efficiency. We find that the classical phase of heaving leading pitching is optimal for power output when the reduced pitching frequency is small (or the fluid stream is fast). At higher pitching frequencies an in-phase response is favored, and maximizes trailing edge deflection. The opposite phase difference minimizes trailing edge deflection and maximizes efficiency.

## References

- [1] G.K. Batchelor, An Introduction to Fluid Dynamics, Cambridge University Press, Cambridge, 1967.
- [2] R. Krasny, Desingularization of periodic vortex sheet roll-up, J. Comp. Phys. 65 (1986) 292–313.
- [3] C.S. Peskin, The immersed boundary method, Acta Numer. 11 (2002) 479–517.
- [4] L. Zhu, C.S. Peskin, Simulation of a flapping flexible filament in a flowing soap film by the immersed boundary method, J. Comp. Phys. 179 (2002) 452–468.
- [5] B.E. Griffith, C.S. Peskin, On the order of accuracy of the immersed boundary method: higher order convergence rates for sufficiently smooth problems, J. Comp. Phys. 208 (1) (2005) 75–105.
- [6] L. Rosenhead, The point vortex approximation of a vortex sheet, Proc. Roy. Soc. London Ser. A 134 (1932) 170–192.
- [7] R. Krasny, Computation of vortex sheet roll-up in the Trefftz plane, J. Fluid Mech. 184 (1987) 123–155.
- [8] D.I. Pullin, The large-scale structure of unsteady self-similar rolled-up vortex sheets, J. Fluid Mech. 88 (03) (1978) 401–430.
- [9] D.W. Moore, The spontaneous appearance of a singularity in the shape of an evolving vortex sheet, Proc. R. Soc. Lon. A 365 (1720) (1979) 105–119.
- [10] P. Saffman, Vortex Dynamics, Cambridge University Press, Cambridge, 1992.

- [11] R. Krasny, Vortex sheet computations: roll-up, wakes, separation, *Lectures Appl. Math.* 28 (1991) 385–402.
- [12] M. Jones, The separated flow of an inviscid fluid around a moving flat plate, *J. Fluid Mech.* 496 (2003) 401–405.
- [13] B. Thwaites, *Incompressible aerodynamics: an account of the theory and observation of the steady flow of incompressible fluid past aerofoils, wings, and other bodies*, Dover, New York, 1987.
- [14] R.K. Shukla, J.D. Eldredge, An inviscid model for vortex shedding from a deforming body, *Theoretical Comput. Fluid Dyn.* 21 (5) (2007) 343–368.
- [15] S. Alben, M.J. Shelley, Flapping states of a flag in an inviscid fluid: bistability and the transition to chaos, *Phys. Rev. Lett.* 100 (2008) 074301.
- [16] S. Alben, Optimal flexibility of a flapping appendage at high Reynolds number, *J. Fluid Mech.* 614 (2008) 355–380.
- [17] S.S. Antman, *Nonlinear Problems of Elasticity*, Springer-Verlag, 1995.
- [18] M.J. Lighthill, Hydromechanics of aquatic animal propulsion, *Annu. Rev. Fluid Mech.* 1 (1969) 413–446.
- [19] N. Didden, On the formation of vortex rings: rolling-up and production of circulation, *Zeitschrift für Angewandte Mathematik und Physik (ZAMP)* 30 (1) (1979) 101–116.
- [20] D.I. Pullin, A.E. Perry, Some flow visualization experiments on the starting vortex, *J. Fluid Mech.* 97 (1980) 239–255.
- [21] M. Nitsche, R. Krasny, A numerical study of vortex ring formation at the edge of a circular tube, *J. Fluid Mech.* 276 (1994) 139–161.
- [22] D.I. Pullin, Z.J. Wang, Unsteady forces on an accelerating plate and application to hovering insect flight, *J. Fluid Mech.* 509 (2004) 1–21.
- [23] N.I. Muskhelishvili, *Singular integral equations: boundary problems of function theory and their application to mathematical physics*, P. Noordhoff, 1953.
- [24] M.A. Jones, M.J. Shelley, Falling cards, *J. Fluid Mech.* 540 (2005) 393–425.
- [25] M. Shelley, N. Vandenbergh, J. Zhang, Heavy flags undergo spontaneous oscillations in flowing water, *Phys. Rev. Lett.* 94 (2005) 094302.
- [26] M.J. Lighthill, Note on the swimming of slender fish, *J. Fluid Mech.* 9 (2) (1960) 305–317.
- [27] T.Y.T. Wu, Swimming of a waving plate, *J. Fluid Mech.* 10 (3) (1961) 321–344.
- [28] J.M. Anderson, K. Streitlien, D.S. Barrett, M.S. Triantafyllou, Oscillating foils of high propulsive efficiency, *J. Fluid Mech.* 360 (1998) 41–72.
- [29] A. Ralston, P. Rabinowitz, *A First Course in Numerical Analysis*, Dover, 2001.
- [30] J.A.C. Weideman, S.C. Reddy, A matlab differentiation matrix suite, *ACM Transactions on Mathematical Software*, 26, 465–519.
- [31] J.C. Mason, D.C. Handscomb, *Chebyshev Polynomials*, Chapman & Hall, 2003.
- [32] M.A. Golberg, *Numerical Solution of Integral Equations*, Plenum Press, New York, 1990.
- [33] C.P. Ellington, C. Vandenberg, A.P. Willmott, A.L.R. Thomas, Leading-edge vortices in insect flight, *Nature* 384 (6610) (1996) 626–630.
- [34] L.A. Segel, *Mathematics Applied to Continuum Mechanics*, Macmillan Publishing Co., New York, 1977.
- [35] K. Isogai, Y. Shinmoto, Y. Watanabe, Effects of dynamic stall on propulsive efficiency and thrust of flapping airfoil, *AIAA J.* 37 (10) (1999) 1145–1151.
- [36] M.J. Lighthill, Aquatic animal propulsion of high hydrodynamic efficiency, *J. Fluid Mech.* 44 (1970) 265–301.
- [37] T.Y. Wu, Hydromechanics of swimming propulsion. Part 2. Some optimum shape problems, *J. Fluid Mech.* 46 (1971) 521–544.
- [38] Z.J. Wang, The role of drag in insect hovering, *J. Exp. Biol.* 207 (23) (2004) 4147–4155.
- [39] T.Y. Wu, Hydromechanics of swimming propulsion. Part 1. Swimming of a two-dimensional flexible plate at variable forward speeds in an inviscid fluid, *J. Fluid Mech.* 46 (2) (1971) 337–355.